Materials Science & Engineering A 978 (2026) 151115

Contents lists available at ScienceDirect

Materials Science & Engineering A

journal homepage: www.elsevier.com/locate/msea

From quasi-static to dynamic loading: Temperature and density effects in flexible silica aerogels

Max Hopp-Zinke [a,c], Christian Weißelberg [a,b], Barbara Milow [a,b], Gunnar Seide [c], Ameya Rege [a,d,*]

[a] Institute for Frontier Materials on Earth and in Space, German Aerospace Center (DLR), Linder Höhe, Cologne, 51147, Germany
[b] Institute of Inorganic and Materials Chemistry, University of Cologne, Greinstraße 4–6, Cologne, 50939, Germany
[c] Aachen-Maastricht Institute for Biobased Materials (AMIBM), Maastricht University, Urmonderbaan 22, Geleen, 6167 RD, The Netherlands
[d] Department of Mechanics of Solids, Surfaces & Systems, University of Twente, P.O. Box 217, Enschede, 7500 AE, The Netherlands

ARTICLE INFO

Keywords:
Marshmallow aerogel
Density
Elastic modulus
Power-law
Dynamic
Complex modulus
Cryogenic

ABSTRACT

Flexible silica aerogels are highly porous lightweight materials with a unique flexibility, rendering them suitable for multifunctional applications in diverse fields, including aerospace and energy storage. However, such applications generally demand cryogenic conditions that require elastic flexibility and mechanical stability across a wide range of temperatures and dynamic mechanical stresses. This study investigates the viscoelastic behaviour of flexible silica aerogels as well as the impact of tunable synthesis parameters, such as dilution and aging time, under dynamic mechanical and cryogenic conditions. Quasi-static testing revealed enhanced stiffening of the aerogels with increasing density as well as with decreasing temperature. The results further demonstrate power-scaling relations between the elastic modulus and density, with exponents ranging between 2–3 for long-aged samples, but extraordinarily 5–8 for short-aged ones. Dynamic mechanical analysis (DMA) revealed low energy dissipation and minor temperature sensitivity, suggesting that flexible silica aerogels have potential applications in aviation or liquefied gas storage. The quasi-static and dynamic mechanical response could be tailored towards lower densities without sacrificing material stiffness by increasing aging time. Storage modulus peaks as well as differential scanning calorimetry (DSC) results both indicate short-term stiffening around −100 to −150 °C. This phenomenon can be hypothesised to be related to glass transitions or nitrogen interaction. It is recommended that further combined DMA and DSC studies are conducted to fully harness the potential of flexible silica aerogels in practical cryogenic applications.

1. Introduction

Aerogels are lightweight and highly porous nanostructured materials. They exhibit a large range of exceptional properties, including low density and a high inner specific surface area [1]. First developed in 1931 through an innovative supercritical drying procedure by Kistler [2], the subject of aerogels has been a long-standing area of research and to date, they continue to offer solutions to a wide range of challenges, including thermal and acoustic insulation, energy storage, medical applications and aerospace engineering [3–7]. Moreover, aerogels can be made out of various precursors like organic, inorganic or bio-based materials thereby making it possible to better address challenges arising with certain applications. In particular, silica aerogels have demonstrated the ability to effectively address numerous commercial demands, owing to their tailorable physicochemical characteristics [8]. However, silica aerogels, which are commonly synthesised with silicon alcoxides as precursors, such as tetramethylorthosilicate (TMOS) or tetraethylorthosilicate (TEOS), typically exhibit a high degree of brittleness, which limits their practical application. In order to address this challenge, various efforts have been made to develop more flexible versions of silica aerogels. These exhibit enhanced flexibility due to the usage of less crosslinkable precursors.

One promising flexible silica aerogel made from methyltrimethoxysilane (MTMS) and dimethyldimethoxysilane (DMDS), now commonly referred to as "marshmallow aerogels" (MGs), was first introduced by Hayase et al. [9] based on the previous work of Nadargi et al. [10]. MGs offer solutions for numerous applications, such as the creation of large scale vesicles for drug delivery [11] or utilising their hydrophobicity for oil separation in ocean cleaning [12]. Their properties can be tuned even further by varying precursor ratios [13] or by developing composite materials [14,15]. However, their multifunctionality makes

* Corresponding author at: Department of Mechanics of Solids, Surfaces & Systems, University of Twente, P.O. Box 217, Enschede, 7500 AE, The Netherlands.
E-mail address: ameya.rege@utwente.nl (A. Rege).
URL: https://people.utwente.nl/ameya.rege (A. Rege).

https://doi.org/10.1016/j.msea.2026.151115
Received 22 January 2026; Received in revised form 11 September 2026; Accepted 17 September 2026
Available online 3 October 2026
0921-5093/© 2026 The Authors. Published by Elsevier B.V. This is an open access article under the CC BY license (http://creativecommons.org/licenses/by/4.0/).

them particularly interesting for cryogenic applications. Due to their aerogel-typical high porosity combined with their flexible nature, they can adsorb and release nitrogen like a sponge [12]. During this process, their surface hydrophobicity prevents damage from ice crystal formation, making them suitable for cryogenic applications such as hydrogen storage or the cold storage of, for example, embryos [16].

Furthermore, increasing the water-to-precursor ratio of MGs can lower their bulk density. It was shown by Steffens et al. [17] that decreasing the density of MGs does not significantly affect their thermal conductivity, as the pores in standard ratio MGs are already larger than the mean free path of air molecules, which are the primary contributors to the gaseous component of heat transfer. This lightweight characteristic further enhances the appeal of MGs for aerospace applications, where weight is a crucial factor. Another tunable parameter is the aging time of the gels after gelation, as unreacted precursors can further connect the porous structure of the network, potentially increasing its mechanical stability. This is coupled with the downside of longer processing time, a crucial factor, especially when considering potential industrial-scale applications. However, for practical cryogenic or aerospace applications the MGs need to maintain a certain elastic flexibility over a broad temperature range, down to −55 °C for commercial aircraft [18] or even lower for energy applications like liquid hydrogen storage [19,20]. Additionally, MGs would be subjected to vibrations during flights, which can have dramatic effects on their long-term mechanical performance. Therefore, a mechanical evaluation of the viscoelastic behaviour of MGs under these conditions is necessary.

In our previous work [21], we demonstrated a method for the mechanical characterisation of aerogels with reproducible shape, including the usage of specific moulds, 3D scanning and digital image correlation. While this approach shows the potential of state-of-the-art techniques for mechanical characterisation of MGs in standard applications, it does not provide insights into their viscoelastic behaviour. Therefore the question arises: How do MGs behave under combined dynamic mechanical and cryogenic conditions, and how might variations in density and aging affect their mechanical behaviour? In this paper, the results of dynamic mechanical analysis (DMA) on MGs with varying densities and aging times are presented and discussed. DMA involves applying an oscillating stress to a sample and recording their corresponding deformation, allowing the complex modulus (comprising storage and loss modulus) to be evaluated. While few studies focused on stiffer silica aerogels or their composites [22], the low mechanical stiffness of MGs and their diluted variations may reveal thermal effects, such a glass transitions. For MGs, a potential glass transition could be expected in the region of −130 °C, although the literature presents differing claims on this subject [12,16]. To thoroughly understand and discuss the viscoelastic behaviour, differential scanning calorimetry (DSC), a technique that can track phase changes through heat consumption, was also performed.

2. Methods

2.1. Synthesis

The synthesis of MGs followed the protocol by Fener and Niemeyer [23], whereas the dilution strategy was adapted from the work of Steffens et al. [17]. Demineralised water (39.65/50.00/65.00 mol equivalents relative to MTMS) and urea (3.97 eq.) were mixed in a beaker and heated to 50 °C. Once the temperature was reached, glacial acetic acid (0.004 eq.) was added. The solution was stirred for 5 min, after which MTMS (1.0 eq.) and subsequently a hexadecyltrimethylammonium chloride solution (25 wt% in water) (0.15 eq.) were added. Stirring was continued for an additional 15 min before DMDMS (0.67 eq.) was added. The mixture was then stirred for another 45 min. The hydrolysed sol was transferred to a mould container consisting of a drilled polypropylene plate, clamped in between two further plates. Contact areas were sealed using flexible tape made of EPDM rubber and PTFE coated paper foil inlets were placed inside the container to avoid adhesion of the MG mats (see Fig. 1a). Afterwards, the container was placed in an oven at 80 °C for 1 or 7 days. Subsequently, the mat was demoulded and placed in a vessel for washing in four steps with 24 h each. The first two steps were done in demineralised water, then once with ethanol and one last time with demineralised water. After confirming the absence of impurities in the washing solvents, the mat was dried under ambient pressure in an oven at 80 °C for 24 h. The resulting samples and their characteristic synthesis properties are displayed in Table 1. Given the expected tendency towards lower densities for higher dilutions, the samples were named LD (low density), MD (medium density) and HD (high density) respectively.

Table 1
Sample name with synthesis and aging parameters.

Sample name	H_2O:MTMS molar-ratio	Aging time [days]
HD_1d	39.65	1
MD_1d	50.00	1
LD_1d	65.00	1
HD_7d	39.65	7
MD_7d	50.00	7
LD_7d	65.00	7

2.2. Structural characterisation

Following the drying process, the samples were carefully cut into cubes with a side length of 6 mm using razor blades (*Classic Sword, Wilkinson*) as shown in Fig. 1a. Subsequently, their geometric properties (cube side lengths and volume) were captured utilising a 3D scanner (*GOM ATOS Q, Zeiss*) equipped with 100 MV lenses. Finally, the mass of each sample was measured with a precision scale (*MS104S/03, Mettler Toledo*) to allow for determining bulk densities. To examine the effects of precursor-dilution on the porous network, scanning electron microscopy was performed (*ULTRA55, Carl Zeiss AG*). Prior to imaging, samples were sputter-coated with platinum for 100 s at a voltage of 21 mA (*SCD-050, BalTec AG*). Images were acquired at an acceleration voltage of 3 kV and a working distance ranging from 7.6 to 9.3 mm.

2.3. Dynamic and quasi-static mechanical tests

Mechanical testing was conducted (*DMA01, Mettler Toledo*) utilising a 10 N loading cell and a 35 litre liquid nitrogen (LN_2) dewar. These devices were coupled to an automated regulation system that controlled the temperature through heating rods of the DMA01 test chamber or via valves regulating the LN_2 flooding. The DMA was set up in compression mode with fixed spacers to achieve a free sample length of precisely 6 mm for clamping the previously synthesised MG cubes (see Fig. 1a and b).

When utilising a DMA, an oscillating strain is applied to the material. Depending on the materials viscoelastic behaviour, the resulting stress given by the materials response will lag behind by a certain phase angle, denoted as δ. For most materials, this phase angle δ typically falls within the range of 0° (purely elastic) to 90° (purely viscous). During an oscillation experiment, the storage modulus E′, loss modulus E″, and $\tan(\delta)$, otherwise referred to as the inner friction of a material, are measured in accordance to

$$E'(\omega) = \frac{\sigma_A}{\epsilon_A}\cos(\delta), \tag{1}$$

$$E''(\omega) = \frac{\sigma_A}{\epsilon_A}\sin(\delta), \tag{2}$$

$$tan(\delta) = \frac{E''}{E'}, \tag{3}$$

where ω is the angular frequency of the DMA. The storage modulus E′ is calculated according to Eq. (1) as a function of the stress amplitude,

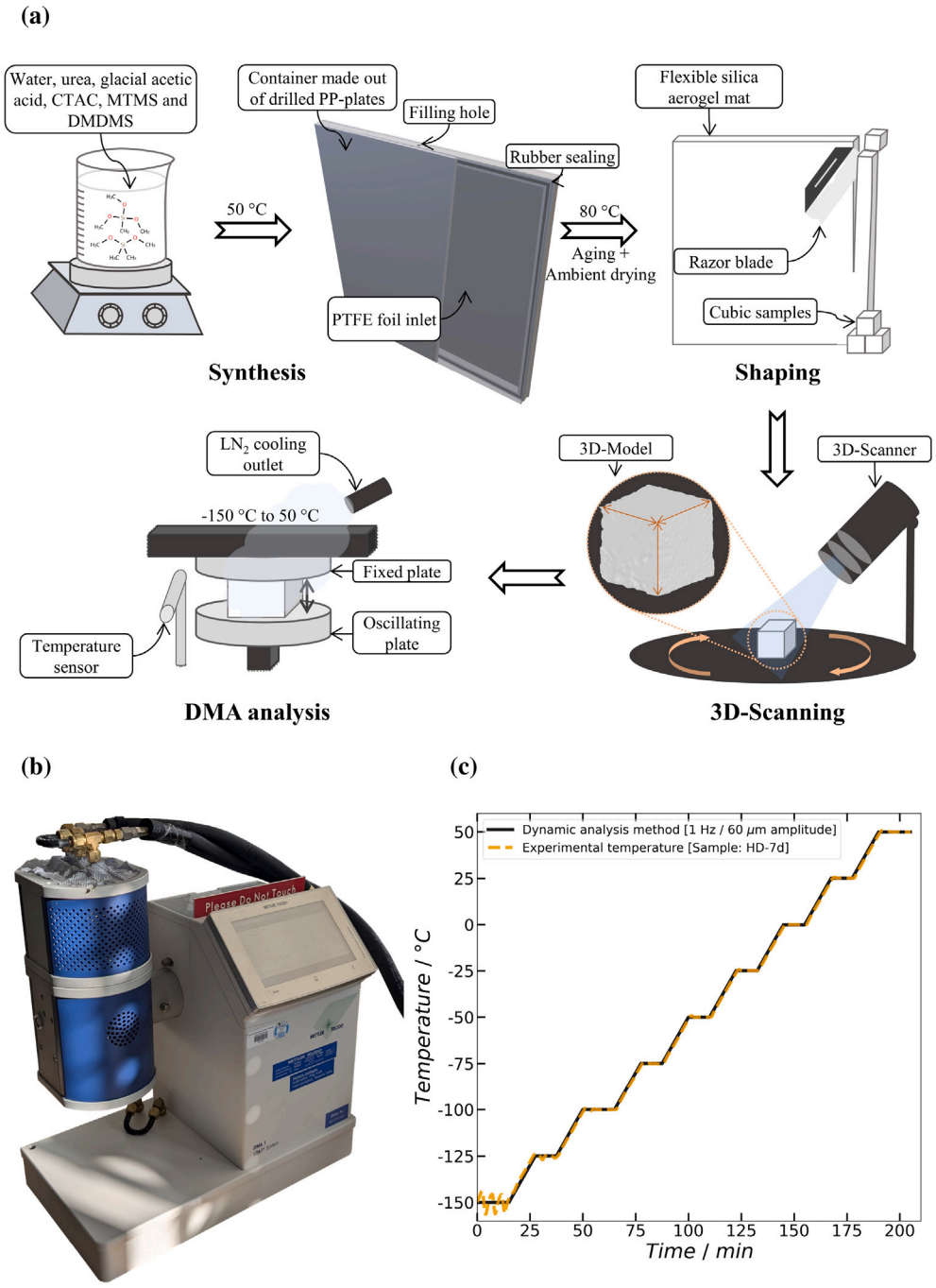


Fig. 1. Methodology of DMA analysis (a) Synthesis of MGs using polypropylene moulds followed by cutting cubic samples with razor blades. Samples are analysed with 3D scanning. DMA is put to compressive mode combined with LN_2 cooling. (b) The DMA01 device running with the oven for cooling and heating locked on top of the sample holder. (c) Temperature profile of the DMA method applied on the cubic MG samples.

denoted by σ_A, and strain amplitude, denoted by ϵ_A, as well as the cosine of the phase angle δ (in-phase with the strain). Consequently, it can be considered a representative measure for the reversible energy stored within the material during the compression phase. The loss modulus E″ is calculated with Eq. (2) using the sine of the phase angle δ (in-phase with the strain rate). It is representative of the dissipated energy (heat) during a compression phase. Lastly, the tan(δ) is calculated according to Eq. (3) as the ratio of loss to storage modulus. Therefore, it can be regarded as the damping capability of the material.

For the dynamic testing of the MGs using the DMA01 device, the sample was first cooled to −150 °C and held at that temperature for 15 min. This ensured that the temperature measured by the sensor placed next to the sample accurately represented the sample temperature, while also reducing the risk of temperature inhomogeneity. After this holding period, a displacement amplitude of 60 μm (1% compressive strain) at a frequency of 1 Hz was applied to the sample. The displacement amplitude of 60 μm was selected to ensure a dynamic displacement within the linear-elastic stress–strain regime. In contrast, a frequency of 1 Hz enabled slip-free testing of the highly flexible samples, eliminating the need for additional clamping support (e.g., adhesives or tapes) that could influence the results. These consistent, low frequency conditions were prioritised to evaluate the artefact-free effects of aging and density, rather than testing high-frequency series (>15–300 Hz) [24,25] more typical for aviation. The temperature was

then increased at a rate of 2 K/min, with an additional 10 to 15 min holding period every 25 K, until reaching 50 °C. The targeted temperature curve as a function of operating time can bee seen in Fig. 1c. Furthermore, a representative temperature curve recorded during an experiment is presented, which demonstrates satisfactory temperature control, with the exception of temperature regions below −125 °C, where temperature fluctuations of up to ±10 K were observed during holding periods. However, to ensure the results are representative of each temperature step, only data collected after temperature stabilisation periods of at least 10 min was considered for the complete measurement. Over the temperature range from −150 °C to 50 °C, this process resulted in a total of nine measurement points for the storage modulus E', loss modulus E'', and tan(δ).

To better understand the impact of dynamic loading on MGs, additional quasi-static testing was performed for comparison under the same conditions. For this, each sample was first clamped and cooled down to −150 °C. After a 15 min holding period, a quasi-static displacement was applied with a force rate of 0.1 N/min for 5 min. From there, samples were decompressed and the temperature was changed to −100 °C and finally to −50 °C, by a combination of reduced LN_2 flooding and heating rods. At each temperature step, the same procedure and measurement used at −150 °C was repeated.

For both quasi-static and dynamic mechanical testing, a minimum of three samples of each type were tested to ensure statistical accuracy.

3. Results and discussion

3.1. Morphology and density

The acquired SEM images are depicted in Fig. 2. The pictures illustrate the porous network of the high (Fig. 2a), medium (Fig. 2b) and low density samples (Fig. 2c) both with and without additional aging time (left: 1 day and right: 7 days). All pictures present the porous structure of the MG samples, which consists of spherical particles interconnected through inter-particle neck regions. For quantitative assessment, the mean particle sizes, derived from 10 randomly selected particles per image and the corresponding standard deviation are presented in Table 2. Here, mean particle sizes for short-aged samples (1d type) range from 5.5 to 6.5 μm, decreasing with higher dilution as expected. Correspondingly, increasing dilution leads to decreasing bulk density, which can be attributed to the distribution of a constant quantity of MTMS and DMDMS precursors across a increasing volume via water dilution, which aligns with the findings of Steffens et al. [17]. However, given the subtle nature of the particle size differences, which largely fall within the standard deviation, they are barely distinguishable in the SEM images. Nonetheless, one notable visual distinction is evident in the particle surfaces of the LD samples. Closer inspection at higher magnification (see Fig. 2c) reveals that the visible secondary particles accounted for in particle size derivation are agglomerated with numerous smaller ones (primary particles). This suggests that, for these lower densities, a one-day aging period may be insufficient for a uniform condensation leading to incoherent particle clusters. A potential explanation for this observation can be found in the reduced probability of particles to collide with each other, which can be attributed to the constant precursor diluted over a higher volume. Consequently, condensation reactions would be less efficient, thus limiting the potential for smaller particles to bridge into larger ones.

In comparison to the 1d samples, the mean particle sizes of the long-aged samples (7d type) appear to be slightly smaller with values ranging from 5.2 (LD and MD) to 5.4 μm (HD). This observation seems counterintuitive, as one would expect longer aging times to result in the fusion of particles into larger ones during the aging process. This fusion effect is indeed visible for both MD_7d and LD_7d samples. In the case of MD_7d samples, secondary particles appear smoother with fewer primary particles adhering to them compared to MD_1d samples. For the LD samples, this phenomenon is especially pronounced, as evidenced by the substantial decrease in the number of primary particles that are discernible for the LD_1d sample. These primary particles have coalesced into secondary particles during prolonged aging, which then exhibit rougher surfaces indicative of the primary particles from which they originated. These observations further suggest limited condensation resulting from higher dilution, even after 7 days aging. The mean particle size being slightly lower for samples of higher aging times might therefore be explained by two different factors. Firstly, the secondary particles appear to be sufficiently large and comparable to only allow for a marginal size gradient. Consequently, minor increases in the neck region would then result in the merging of two particles to such a small extent that the neck region undergoes only minor expansion. This effect could lead to the appearance of both particles as being reduced in size, owing to the material merging into the neck region. Secondly, in the case of LD, the highest size gradient is exhibited by the primary particles that are visible prior for LD_1d. These particles now merge incompletely into secondary particles, resulting in a non-spherical shape that would most likely distort the accuracy of particle size measurement. Considering these potential influences and the minor particle size differences, which largely fall within the

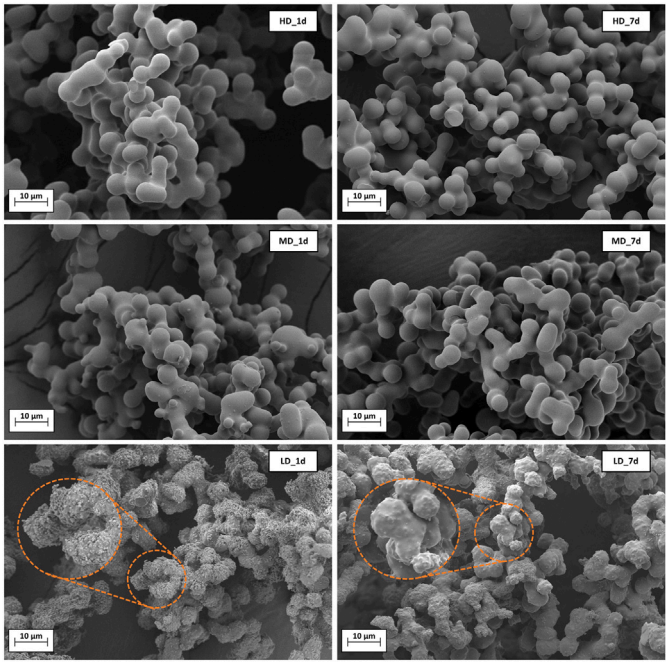


Fig. 2. Porous network of the different dilution-aging combinations captured through scanning electron microscopy: (a) High density samples with 1 and 7 days of aging time (39.65 molar ratio H_2O:MTMS); (b) Medium density samples with 1 and 7 days of aging time (50.00 molar ratio H_2O:MTMS); (c) Low density samples with 1 and 7 days of aging time (65.00 molar ratio H_2O:MTMS).

Table 2
Mean particle sizes of various MG dilution-aging combination samples (10 particles per picture) with equivalent standard deviations.

	H2O:MTMS molar ratio	Envelope density [g/cm^3]	Mean particle size [μm]
HD_1d	39.65	0.098	$6.5_{\pm 1.1}$
MD_1d	50.00	0.088	$5.7_{\pm 0.9}$
LD_1d	65.00	0.068	$5.5_{\pm 0.6}$
HD_7d	39.65	0.103	$5.4_{\pm 0.8}$
MD_7d	50.00	0.089	$5.2_{\pm 1.0}$
LD_7d	65.00	0.067	$5.2_{\pm 0.9}$

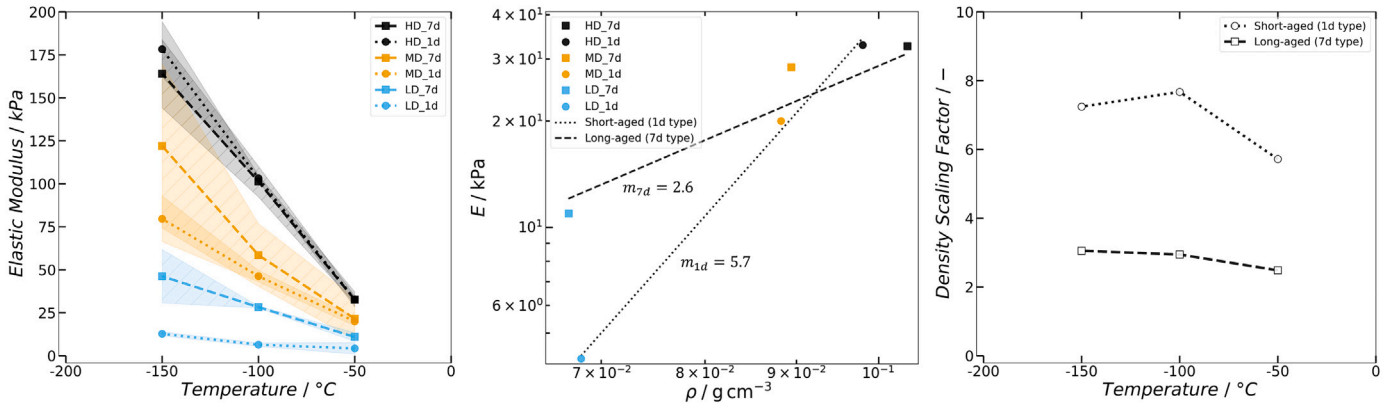


Fig. 3. Results of quasi-static compressive testing: (a) Elastic modulus captured at a compressive state of 60 µm (1% compressive strain) as a function of temperature (including highlighted areas indicating standard deviation resulting from tests in triplicate); (b) Elastic modulus (short: E) at −50 °C as a function of the envelope density (short: ρ) on a double logarithmic scale including two trendlines for aging classes based on the logarithmically transformed data; (c) Density scaling factor of two aging classes as a function of temperature. (For interpretation of the references to colour in this figure legend, the reader is referred to the web version of this article.)

standard deviation, significant changes in the porous structure due to additional aging appear to be primarily evident in lower densities, particularly the LD samples.

3.2. Quasi-static testing

The results for quasi-static testing are presented in Fig. 3a, illustrating the elastic modulus as a function of temperature. To determine elastic modulus, the slope is calculated at 60 µm quasi-static compression (1% compressive strain). The various curves represent combinations of density class and aging time, measured at three temperature points ranging from −150 to −50 °C. For each combination, one representative sample out of triplets, closely approximating the mean value, is depicted. Additionally, standard deviations derived from multiple measurements are indicated by similarly coloured areas surrounding the curves. It is evident that all curves demonstrate an increase in elastic modulus with decreasing temperature. The highest elastic modulus values are obtained by HD_1d and 7d samples, ranging from 35 kPa to 167 kPa, while the lowest values are observed for the LD_1d sample, with values between 8 kPa and 14 kPa. It is visible that MGs of greater density exhibit higher elastic moduli, as do longer aged samples when compared to their shorter aged counterparts. Furthermore, the slope of the elastic modulus curves appears steeper for higher density class combinations.

The increase of elastic modulus with decreasing temperature aligns with expectations, which can be most likely be traced back to low-temperature stiffening resulting in reduced molecular mobility. The increased stiffness observed for higher densities is also anticipated, as a more interconnected porous structure could result in a more robust solid backbone structure. This expectation is supported by SEM image comparisons of low to high density samples, which revealed differences in condensation progress, especially between HD and LD samples. Notably, variations in the particle size for LD samples between secondary and smaller primary particles may limit connectivity and solidity of the solid backbone structures, thus explaining stiffness differences. This observation would also add to the findings of Steffens et al. [17] but expands upon them by adding temperature sensitive data, revealing a more significant difference evident in the cold temperature region. Here, values exhibit more substantial variation, with the elastic modulus of LD_1d increasing by approximately 75% between −50 to −150 °C, while the modulus of HD_7d increases by nearly 380%. Consequently, lower density MGs demonstrate a more stable mechanical response under cryogenic conditions, most likely due to their previously mentioned limited condensation.

Similarly, long-aged samples generally exhibit increased elastic moduli compared to short-aged samples of the same density. However, while this effect is most pronounced for LD samples, it appears to diminish with increasing density, even falling within the standard deviation for the majority of MD and HD data. This observation implies that aging induces a more pronounced and temperature-sensitive stiffening effect in lower-density samples compared to their higher-density counterparts. This disparity could be ascribed to aging exerting a less substantial influence on the pore structure of higher-density samples and, consequently, on their solid backbone, as evidenced by the SEM images (see Fig. 2). In the case of lower-density samples, a higher chemical potential resulting from larger particle size gradients can be anticipated, potentially leading to increased influence of aging phenomenons like ostwald ripening after prolonged aging and condensation of primary particles. However, as previously explained, the condensation of LD samples is ultimately constrained, possibly due to statistically reduced particle collisions. Consequently, the LD samples are characterised by weaker neck regions, which may also contribute to their reduced sensitivity to low-temperature stiffening, as a lower particle–particle cross section further reduces the heat transfer through the solid.

The relationship between stiffness and density can also be quantified using the power-law scaling exponent. Several authors have investigated this modulus-density relationship for less flexible materials [26–28]. The normalised elastic modulus, denoted as E, scales with density ρ according to

$$E = C\rho^m, \tag{4}$$

where C represents a structure dependent scaling coefficient while m represents the scaling exponent. Such a power-law relationship for the flexible MGs is illustrated in Fig. 3b for the representative case of −50 °C. Here, the mean elastic modulus for each density-aging combination is plotted as a function of the envelope density in a double logarithmic scale. Accordingly, two trendlines are fitted, each corresponding to a different aging class. These trendlines indicate that the density dependence of the elastic modulus becomes softer and more towards the expected 2–4 range of aerogels, as quantified by m, upon pronounced aging.

As illustrated in Fig. 3c, for long-aged samples, m increases from 2.5 to approximately 3 as temperatures decrease. Conversely, short-aged samples exhibit a higher scaling factor, ranging from 5.7 to almost 8. The long-aged samples align with established literature values for standard silica aerogels, where scaling exponents typically range from 2 to 4 (see [28,29]). However, the higher values observed for short-aged samples can be attributed to the pronounced aging effect in

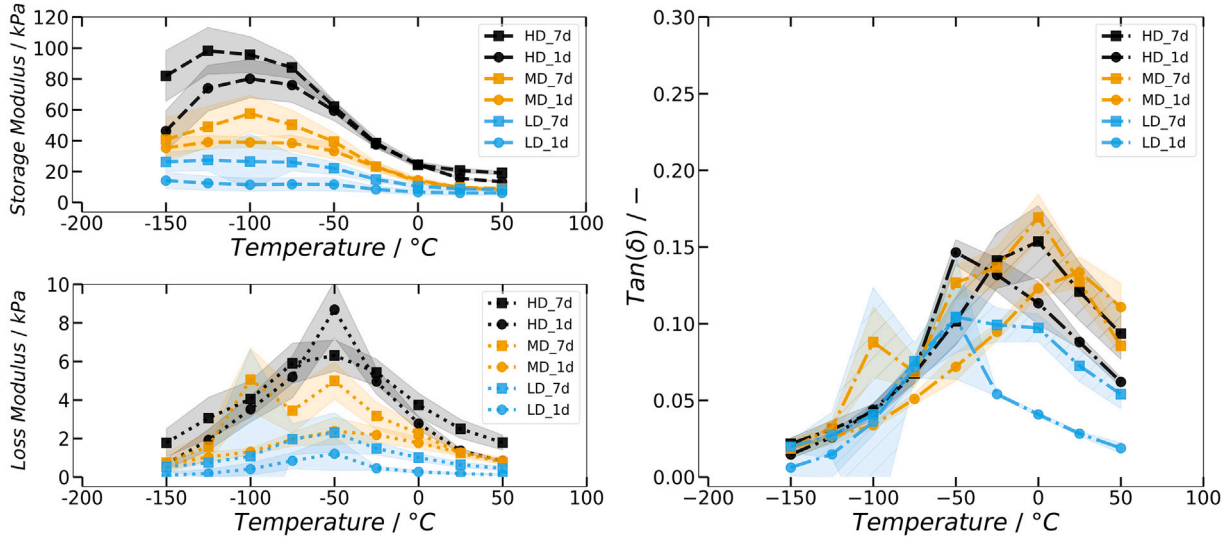


Fig. 4. Results of dynamic compressive testing at a fixed frequency of 1 Hz (a) Storage and loss modulus as a function of temperature (b) Tan(δ) as a function of temperature.

low-density samples, as well as the amplified differences between long- and short-aged samples, which become more significant at lower temperatures due to low-temperature stiffening across all density classes. Inter-particle necks alone were shown previously to have no influence on the scaling exponent for open-porous materials [28]. On the other hand, it has also been shown that a bending dominated deformation of woodpile lattices exhibits a power-law exponent of 5 [30]. This behaviour was observed when the lattice spacing was significantly larger than the diameter of the woodpiles. It is therefore a combination of the topology, meaning that there may be significant network rearrangements between short- and long-aged samples, and the then still-cluster of primary particles within the non-homogeneous secondary particle, that results in the very high exponents ranging between 5 and 8. A comprehensive derivation of the power-law scaling and corresponding results are available in the supplementary information (Appendix A).

3.3. Dynamic testing

Fig. 4 illustrates the results of dynamic mechanical testing performed with the DMA. Fig. 4a presents the storage E′ and loss modulus E″ as a function of temperature for the different density and aging combinations. As the temperature increases, most samples, except LD_1d, exhibit an initial rise in storage modulus, reaching a peak between −125 and −75 °C, followed by a decline until 50 °C. Consistent with the quasi-static measurements, the highest modulus values are achieved with higher density and aging time, with storage modulus values ranging from 6 kPa to 19 kPa at 50 °C and from 14 kPa to 82 kPa at −150 °C. The aforementioned peak is most pronounced for HD_7d sample and appears less prominent with reduced density and aging time, nearly disappearing for the M_1d, LD_7d and LD_1d samples. In addition to storage modulus, Fig. 4a also shows the loss modulus. The loss modulus curves are characterised by a single peak around −50 °C for all density–aging combinations, except MD_7d, which exhibits an additional loss modulus peak at −100 °C. This peak appears to be an outlier, as it was not reproducibly observed in other samples of the same type. The highest loss modulus values are associated with higher densities and aging times, with individual peak values ranging from 1 kPa (LD_1d) to 6 kPa (LD_7d). Compared to the storage moduli, the loss moduli are approximately one order of magnitude lower for each density and aging combination.

As observed in the quasi-static measurements, the increase in storage modulus, indicative of rising elastic stiffness, is influenced by cold temperature stiffening of the porous networks. Interestingly, a comparison of the loss modulus at 50 °C and −150 °C, representing energy dissipation during deformation, reveals comparable data. This suggests that the network response for these two strongly differing temperature values remains nearly equally flexible. One possible explanation is the low crosslinked nature of the MGs, which compensates for potential network stress, even with reduced molecular movement at cold temperatures. However, as mentioned before, a distinct peak in the elastic modulus occurs around −100 °C, accompanied by a corresponding peak in the loss modulus around −50 °C with both peaks becoming particularly prominent for higher densities and longer aging combinations. Generally, rapid changes in storage modulus with an equivalent peak in loss modulus during DMA measurements strongly indicate glass transitions. These transitions are typical of amorphous materials, which possess the random structure of liquids but exhibit the viscosity of solids. Such transitions depend on the ability of molecules to move freely, which is reduced at colder temperatures until they begin behaving as brittle solids with reduced damping or deformation capacity. However, two primary reasons suggest that the DMA results presented herein do not conclusively indicate a glass transition. Firstly, reversible glass transitions observed via DMA typically result in a permanent, reversible offset in storage modulus. In contrast, the data illustrate a decrease in elastic modulus after its peak in both temperature directions, particularly for samples with higher densities and longer aging times. Only the samples with shorter aging times and lower densities appear to meet the typical criterion of a permanent offset associated with a glass transition. Secondly, the loss modulus does not peak directly at the same point where the storage modulus undergoes its inflection point. Instead, it appears shifted or delayed. One potential explanation for the rise and decline of storage modulus over this wide temperature range, as well as the delayed response of loss modulus, could be the flexible porous structure of the MGs. This structure may slow down and prevent a uniform transition to a glassy state, potentially due to its insulating properties coupled with the MG typical minor crosslinked network.

As previously mentioned, the existing literature presents differing claims regarding the glass transition of MGs, with Hayase and Ohya [16] suggesting a potential glass transition around −130 °C. In comparison to the DMA data gathered, this aligns somewhat with the lowest temperature of the broad temperature range covered by the storage modulus peak. However, the literature provides no real supporting data yet. To this end, DSC measurement was performed

with the HD_7d sample, as it exhibits the highest change in storage modulus, as well as the most prominent peak. While these DSC results do illustrate a change in the heat flow curve around −130 °C, they did not reflect the typical rapid change expected for a clear glass transition indication. Furthermore, this would not explain the peak of loss modulus around −50 °C. While DSC, in this instance, does not provide a definitive answer regarding glass transition, a detailed report on the results of this measurement can be found in the supplementary information (Appendix B) to provide a base for further investigations.

Nevertheless, a potential glass transition effect alone would fail to explain the storage modulus declining after its peak around −75 °C and −100 °C, for most of the higher density and aging combinations. One further explanation for this phenomenon might be a potential influence of nitrogen interaction, as the samples are in direct contact with nitrogen inside the DMA chamber. Literature provides indications of this, with descriptions of MGs being able to reversibly fill up with nitrogen [12]. Therefore, potential ad- and desorption effects due to hydrogen bonds and surface tension could influence the materials mechanical response, especially since MGs exhibit a comparable low base stress response. This theory was also posited by Li et al. [31], who reported similar observations for comparable, but more rapid, DMA storage modulus peaks for pure MTMS aerogels. In this context, it could also explain the diminishing peak of storage modulus with decreasing density, namely MD_1d, LD_7d and LD_1d, as the limited condensation of low-density aerogels, as observed previously in the form of SEM images and the effects on quasi-static mechanical response, would result in less efficient nitrogen ad- and desorption due to lower interaction surfaces and interconnectivity.

One final aspect to address from the DMA results is the tan(δ), which represents the ratio of loss to storage modulus. It is illustrated in Fig. 4b as a function of temperature. Across all density and aging combinations, it seems obvious that the value of tan(δ) generally increases with temperature until a peak is observed in the range of −50 to 0 °C. This phenomenon can be attributed to the continuous decline of storage modulus, which occurs concurrently with a peak in loss modulus within this temperature range. While a trend suggesting higher tan(δ) values with increased density and aging time is apparent in higher temperature regions, the progression of all tan(δ) curves converges with decreasing temperature. Additionally, many tan(δ) differences among the various samples fall within the standard deviation, particularly under cryogenic conditions. With tan(δ) serving as an indicator of a materials damping capability, the relatively low values exhibited by the various MGs suggest a high degree of flexibility, with maximum values of 0.17 observed around −50 °C. Consequently, MGs demonstrate suitability for applications where low tan(δ) values contribute to reducing energy loss. However, the influence of density and aging appear less pronounced compared to their effects on storage and loss modulus. The lowest value is observed above 0 °C for LD_1d, which aligns with its previously discussed low loss modulus.

The DMA measurements in the present study were performed at a fixed frequency of 1 Hz to enable a systematic comparison of the effects of temperature, density, and aging time on the viscoelastic response of the MGs. Application-specific assessment would require frequency-sweep measurements over a considerably broader range, together with cyclic fatigue tests to quantify possible stiffness degradation, accumulation of permanent deformation, and changes in energy dissipation under repeated loading. Such investigations are beyond the scope of the present study but constitute an important next step towards qualification of MGs for dynamically loaded environments.

From an application perspective, MGs have garnered attention in the aerospace and cryogenic sectors, and should primarily be considered as lightweight insulation materials rather than as purely load-bearing structural components. In this context, relevant reference materials include glass wool and melamine-resin foams, which are widely used for thermal and acoustic insulation. Typical glass-wool insulation exhibits thermal conductivities in the range of 0.035–0.043 $\mathrm{W\,m^{-1}K^{-1}}$, while lightweight melamine foams show thermal conductivities of approximately 0.035 $\mathrm{W\,m^{-1}K^{-1}}$ and are used for thermo-acoustic insulation, including in transportation applications. The particular advantage of MGs lies in combining very low thermal conductivity (0.030-0.035 $\mathrm{W\,m^{-1}K^{-1}}$) with large mechanical deformability and the ability to retain mechanical functionality at cryogenic temperatures. The mechanical damping capability of the MGs, as quantified by tan(δ) measurements above, is comparable in magnitude to melamine foams [32] and glass wool [33,34]. The present results therefore indicate that MGs may provide an alternative to conventional fibrous or polymeric insulation where low thermal conductivity, flexibility, hydrophobicity, and tolerance to thermally induced deformation are simultaneously required.

4. Conclusion

In this study, flexible silica aerogels, so called marshmallow aerogels (MGs), were successfully synthesised based on methyltrimethoxysilane (MTMS) and dimethyldimethoxysilane (DMDMS) with varying densities and aging times. The gels were directly moulded, to minimise post-processing to preserve their structural integrity and geometrically characterised via 3D scanning. A series of analytical methods were employed to investigate their properties. Scanning electron microscopy (SEM) imaging, facilitated by low-voltage and platinum sputtering, revealed the significant influence of prolonged aging on the porous network structure of low-density samples, highlighting both the potential for microstructural tuning and the limitations of aging, as even after seven days numerous not yet fully integrated primary particles were visible on the secondary particle surfaces of the low density MGs. This suggests that alternative strategies must be experimented with, such as a stepwise dilution or pH adjustments, which may offer further optimisation opportunities.

Furthermore, mechanical characterisation was done on a DMA in both quasi-static and dynamic compressive testing mode. Quasi-static tests, performed at three different cryogenic conditions from −150 °C to −50 °C, demonstrated low temperature stiffening, with the highest elastic modulus and temperature sensitivity observed in MGs of higher density and longer aging time. In contrast, the influence of aging appeared increasingly significant for lower densities, likely due to hindered condensation caused by reduced particle collisions at higher dilutions. Power-law scaling was observed for the elastic modulus vs. density relation. While the long-aged samples exhibited an exponent between 2–3, typical of aerogels, the short-aged samples demonstrated very high scaling exponents in the range between 5–8. Dynamic mechanical tests proved essential in assessing MGs behaviour under dynamic deformations at cryogenic temperatures from −150 °C to 50 °C. DMA characteristic values, storage modulus, loss modulus and tan(δ), reveal a highly elastic response and minor temperature sensitivity at cryogenic conditions, indicating low energy dissipation, particularly for MGs of lower densities.

Considering these findings, MGs can be tailored to specific application not only by adjusting the density but also by subjecting them to aging processes. This allows for enhancing stiffness without compromising the lightweight benefits observed at MGs of lower density. Nevertheless, an unresolved peak of storage modulus around −100 °C, without clear evidence from DMA or differential scanning calorimetry (DSC) regarding potential glass transitions, could hint towards possible short-term stiffening effects due to nitrogen interactions within the structure of MGs of higher density and aging combinations. These observations demand further investigations, including DSC analyses of varying MG densities coupled with frequency dependent DMA studies to strengthen the knowledge on dynamic MGs characteristics and potential glass transition behaviour.

Table A.3
Results of the proportionality calculations between the elastic modulus and density.

	−50 °C		−100 °C		−150 °C	
	1 day aging	7 days aging	1 day aging	7 days aging	1 day aging	7 days aging
Proportional factor C	2.00×10^7	8.88×10^3	5.66×10^9	8.13×10^4	3.53×10^9	1.89×10^5
Scaling factor m	5.72	2.48	7.67	2.94	7.24	3.06

CRediT authorship contribution statement

Max Hopp-Zinke: Writing – original draft, Visualization, Methodology, Investigation, Formal analysis, Conceptualization. **Christian Weißelberg:** Writing – original draft, Visualization, Investigation. **Barbara Milow:** Project administration, Funding acquisition. **Gunnar Seide:** Writing – review & editing, Supervision. **Ameya Rege:** Writing – review & editing, Supervision, Methodology, Funding acquisition, Conceptualization.

Declaration of competing interest

The authors declare that they have no known competing financial interests or personal relationships that could have appeared to influence the work reported in this paper.

Acknowledgments

This work was supported by the project ISBA (Insulation Solutions Based on Aerogels) which received funding from the European Union's Horizon 2020 research and innovation programme under grant agreement number 101082573.

The authors gratefully acknowledge Dr. Thomas Anklam, Dr. Nina Borzecka and Bruno Goncalves for their valuable insights and support that contributed to the development of this work. We thank Prof. Dr. Annette Schmidt for providing access to the DSC and Katharina Schwab as well as Linus Kuckling for their technical support and helpful input regarding its operation.

Appendix A. Density scaling factor

As described in the main article, the elastic modulus of porous materials can typically be related to a density scaling factor according to

$$E = C\rho^m, \tag{A.1}$$

with C being a structure dependent scaling coefficient and m being a scaling factor, acting as a measure of the influence of density on the materials stiffness.

To calculate the scaling factor m, the logarithm of the equation was formed according to

$$\ln(E) = \ln(C) + m \cdot \ln(\rho). \tag{A.2}$$

Finally, linear regression was used to calculate the proportional factor C (exponential of the intercept) and the scaling factor m (slope) accordingly. The full results are shown in Table A.3.

Appendix B. Differential scanning calorimetry

The DSC measurements were conducted on a DSC821e instrument (*Mettler Toledo*). Initially, the sample HD_7d, having the most pronounced peak of storage modulus, was heated to 100 °C to negate the possible influence of moisture. Subsequently, it was cooled and subjected to two thermal cycles between −80 °C and −150 °C. The resulting heat flow from the second cycle is presented in Fig. B.5 as a function of temperature, illustrating the heat flow curve during both cooling and heating phases within the specified temperature range.

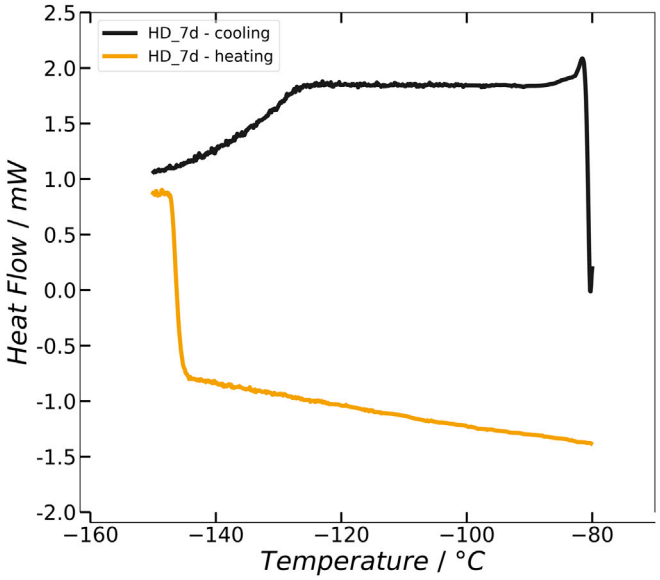


Fig. B.5. Heat flow of HD_7d sample captured during differential scanning calorimetry as a function of temperature.

During the cooling phase, the heat flow remains mostly constant after an initial sharp increase, followed by a gradual decrease from around −130 °C to −150 °C, the end of the cooling phase. Conversely, during the heating phase, the heat flow exhibits a distinct drop around −145 °C before continuing a slow decline until reaching −80 °C.

While the prominent peak at the onset of the cooling phase is likely attributable to a measurement artifact at the boundary of the preceding cycle, the continuous decline commencing at −125 °C, as well as the sharp decline during the heating phase at −145 °C, may indicate a glass transition. However, analogous to a distinct change in storage modulus, a more abrupt alteration in heat flow would be anticipated for a glass transition. Instead, the heat flow diminishes over a broader temperature range. One possible explanation could be the low interconnectivity of the MGs, which could stall the transition of molecules into a glassy state. Nevertheless, the second potential indicator of a glass transition, manifested as the sharp decline in heat flow during the heating phase, occurs at −145 °C, resulting in a 20 °C discrepancy compared to the cooling phase decline. One possible explanation for this phenomenon could be that the thermal conductivity of the MGs is higher at lower temperatures, thus a homogeneous temperature change would facilitate a more rapid transition. However, considering the 20 °C temperature difference and the previously discussed DMA results differing through suggesting similar processes at −100 °C, the data does not provide a definitive conclusion, as elaborated in the main article. Nonetheless, a further combined investigation of DMA and DSC measurements for the various aging and density combinations could provide more precise clarification on the topic.

Data availability

Data will be made available on request.

References

[1] J. Fricke, Aerogels — highly tenuous solids with fascinating properties, J. Non-Cryst. Solids 100 (1) (1988) 169–173.

[2] S.S. Kistler, Coherent expanded aerogels and jellies, Nature 127 (3211) (1931) 741.

[3] R. Garay Martinez, E. Goiti, G. Reichenauer, S. Zhao, M. Koebel, A. Barrio, Thermal assessment of ambient pressure dried silica aerogel composite boards at laboratory and field scale, Energy Build. 128 (2016) 111–118.

[4] T. Linhares, V.H. Carneiro, M.T. Pessoa de Amorim, L. Durães, A comparative thermoacoustic insulation study of silica aerogels reinforced with reclaimed textile fibres: Cotton, polyester and wool, Gels 9 (7) (2023).

[5] S. Huang, D. Yang, W. Zhang, X. Qiu, Q. Li, C. Li, Dual-templated synthesis of mesoporous lignin-derived honeycomb-like porous carbon/SiO2 composites for high-performance Li-ion battery, Microporous Mesoporous Mater. 317 (2021) 111004.

[6] M. Afrashi, D. Semnani, Z. Talebi, P. Dehghan, M. Maherolnaghsh, Comparing the drug loading and release of silica aerogel and PVA nano fibers, J. Non-Cryst. Solids 503–504 (2019) 186–193.

[7] R. Jin, Z. Zhou, J. Liu, B. Shi, N. Zhou, X. Wang, X. Jia, D. Guo, B. Xu, Aerogels for thermal protection and their application in aerospace, Gels 9 (8) (2023).

[8] S. Ahmad, S. Ahmad, J.N. Sheikh, Silica centered aerogels as advanced functional material and their applications: A review, J. Non-Cryst. Solids 611 (2023) 122322.

[9] G. Hayase, K. Kanamori, K. Kazuki, T. Hanada, Synthesis of new flexible aerogels from MTMS/DMDMS via ambient pressure drying, IOP Conf. Ser.: Mater. Sci. Eng. 18 (3) (2011).

[10] D.Y. Nadargi, S.S. Latthe, H. Hirashima, A.V. Rao, Studies on rheological properties of methyltriethoxysilane (MTES) based flexible superhydrophobic silica aerogels, Microporous Mesoporous Mater. 117 (3) (2009) 617–626.

[11] G. Hayase, S.-i.M. Nomura, Large-scale preparation of giant vesicles by squeezing a lipid-coated marshmallow-like silicone gel in a buffer, Langmuir 34 (37) (2018) 11021–11026.

[12] G. Hayase, K. Kanamori, M. Fukuchi, H. Kaji, K. Nakanishi, Facile synthesis of marshmallow-like macroporous gels usable under harsh conditions for the separation of oil and water, Angew. Chem. Int. Ed. Engl. 52 (7) (2013) 1986–1989.

[13] G. Hayase, Surfactant-free aqueous fabrication of macroporous silicone monoliths for flexible thermal insulation, Bull. Chem. Soc. Japan 94 (9) (2021).

[14] G. Hayase, S.-i.M. Nomura, Macroporous silicone sheets integrated with meshes for various applications, ACS Appl. Polym. Mater. 1 (8) (2019) 2077–2082.

[15] A. Rege, P. Voepel, E. Okumus, M. Hillgärtner, M. Itskov, B. Milow, Temperature-dependent stiffening and inelastic behavior of newly synthesized fiber-reinforced super flexible silica aerogels, Materials 12 (18) (2019) 2878.

[16] G. Hayase, Y. Ohya, Marshmallow-like silicone gels as flexible thermal insulators and liquid nitrogen retention materials and their application in containers for cryopreserved embryos, Appl. Mater. Today 9 (2017) 560–565.

[17] K. Steffens, D. Bialuschewski, B. Milow, Tuning density and morphology of organic-inorganic hybrid-silica aerogels through precursor dilution for lightweight applications, J. Sol-Gel Sci. Technol. 112 (3) (2024) 768–775.

[18] A. Williams, How the latest materials testing methods replicate a range of possible flight conditions, 2025 (30.04.2025) (2023).

[19] Z. Kang, L. Yanzhong, M. Yuan, W. Lei, X. Fushou, W. Jiaojiao, Experimental study on cool down characteristics and thermal stress of cryogenic tank during LN2 filling process, Appl. Therm. Eng. 130 (2018) 951–961.

[20] Y. Ma, K. Zhu, Y. Li, F. Xie, Numerical investigation on chill-down and thermal stress characteristics of a LH2 tank during ground filling, Int. J. Hydrog. Energy 45 (46) (2020) 25344–25356.

[21] M. Zinke, B. Milow, G. Seide, A. Rege, Mechanical structure–property relations in flexible silica-aerogels, Mech. Mater. 211 (2025) 105510.

[22] A. Katti, N. Shimpi, S. Roy, H. Lu, E.F. Fabrizio, A. Dass, L.A. Capadona, N. Leventis, Chemical, physical, and mechanical characterization of isocyanate cross-linked amine-modified silica aerogels, Chem. Mater. 18 (2) (2006) 285–296.

[23] R. Fener, P. Niemeyer, Flexible Komposite auf Basis von Aerogelen, Tech. Rep. EP 3 042 884 B1, European Patent Office, 2016.

[24] J.F. Unruh, D.C. Scheidt, Engine Isolation for Structural Borne Interior Noise Reduction in a General Aviation Aircraft, Report, Southwest Research Inst. San Anonio, 1981.

[25] M.C. Moruzzi, M. Cinefra, S. Bagassi, Vibroacoustic analysis of an innovative windowless cabin with metamaterial trim panels in regional turboprops, Mech. Adv. Mater. Struct. 28 (14) (2021) 1509–1521.

[26] J. Groß, J. Fricke, Scaling of elastic properties in highly porous nanostructured aerogels, Nanostruct. Mater. 6 (5–8) (1995) 905–908.

[27] S. Zhao, W.J. Malfait, N. Guerrero-Alburquerque, M.M. Koebel, G. Nyström, Biopolymer aerogels and foams: Chemistry, properties, and applications, Angew. Chem. Int. Ed. 57 (26) (2018) 7580–7608.

[28] S. Aney, P. Pandit, L. Ratke, B. Milow, A. Rege, On the origin of power-scaling exponents in silica aerogels, J. Sol-Gel Sci. Technol. 114 (1) (2025) 98–105.

[29] S. Iswar, S. Galmarini, L. Bonanomi, J. Wernery, E. Roumeli, S. Nimalshantha, A.M. Ben Ishai, M. Lattuada, M.M. Koebel, W.J. Malfait, Dense and strong, but superinsulating silica aerogel, Acta Mater. 213 (2021) 116959.

[30] E. Cuan-Urquizo, F. Shalchy, A. Bhaskar, Compressive stiffness of staggered woodpile lattices: Mechanics, measurement, and scaling laws, Int. J. Mech. Sci. 187 (2020) 105932.

[31] Y. Li, A. Du, J. Shen, Z. Zhang, G. Wu, B. Zhou, Temperature dependence of dynamic mechanical behaviors in low density MTMS-derived silica aerogel, J. Porous Mater. 25 (4) (2018) 1229–1235.

[32] L. Jaouen, A. Renault, M. Deverge, Elastic and damping characterizations of acoustical porous materials: Available experimental methods and applications to a melamine foam, Appl. Acoust. 69 (12) (2008) 1129–1140.

[33] T. Pritz, Frequency dependence of frame dynamic characteristics of mineral and glass wool materials, J. Sound Vib. 106 (1) (1986) 161–169.

[34] P. Bonfiglio, F. Pompoli, K.V. Horoshenkov, M.I.B.S.A. Rahim, L. Jaouen, J. Rodenas, F.-X. Bécot, E. Gourdon, D. Jaeger, V. Kursch, et al., How reproducible are methods to measure the dynamic viscoelastic properties of poroelastic media? J. Sound Vib. 428 (2018) 26–43.